

Spin-glass ground states in the frustrated pyrochlore and fluorite antiferromagnets NaCdM_2F_7 ($M = \text{Ni}^{2+}, \text{Mn}^{2+}$)

Andrej Kancko,¹ Cinthia Antunes Corrêa,² and Ross Harvey Colman^{1*}

¹ Charles University, Faculty of Mathematics and Physics, Department of Condensed Matter Physics, Ke Karlovu 5, 121 16 Prague 2, Czech Republic

² Institute of Physics of the Czech Academy of Sciences, Na Slovance 2, Prague 8, 182 21, Czech Republic

*Corresponding author: ross.colman@matfyz.cuni.cz

Abstract

We report the crystal structures, magnetic and thermodynamic properties of two magnetically frustrated $A'A''M_2F_7$ -type antiferromagnets, $\text{NaCdNi}_2\text{F}_7$ and $\text{NaCdMn}_2\text{F}_7$. While $\text{NaCdNi}_2\text{F}_7$ forms a stable pyrochlore structure (SG: $Fd-3m$, #227) with magnetic $S = 1$ Ni^{2+} ions on the frustrated pyrochlore 16c site and fully disordered non-magnetic $\text{Na}^+/\text{Cd}^{2+}$ ions on the pyrochlore 16d site, $\text{NaCdMn}_2\text{F}_7$ favors the defect-fluorite structure (SG: $Fm-3m$, #225) with magnetic $S = 5/2$ Mn^{2+} and non-magnetic Na^+ and Cd^{2+} ions fully disordered on the fluorite 4a site. This is a result of the Mn^{2+} ionic radius being too close to the average $\text{Na}^+/\text{Cd}^{2+}$ ionic radius, hindering the cationic site ordering towards the stable pyrochlore structure. In both cases, dominant antiferromagnetic interactions $\theta_{\text{CW,Ni}} = -91.2(5)$ K and $\theta_{\text{CW,Mn}} = -42.4(4)$ K are noted, with no magnetic transition until $T_{f,\text{Ni}} = 3.2$ K and $T_{f,\text{Mn}} = 2.0$ K, implying substantial frustration, with frustration indices $f_{\text{Ni}} = 28.5$ and $f_{\text{Mn}} = 21$. AC susceptibility measurements and bifurcation of ZFC/FC low-field magnetization indicate a glassy ground-state, precipitated by the magnetic-bond-disorder stemming from the inherent structural disorder.

Keywords: pyrochlore, defect-fluorite, spin-glass, frustrated magnetism, nickel, manganese

Introduction

The pyrochlore lattice, a 3D network of corner-sharing tetrahedra, is a prototypical structure for three-dimensional geometrical frustration. The specific vertex-sharing tetrahedral arrangement of spins leads to competing magnetic exchange interactions that prevent the system from achieving a trivial magnetic order. [1,2] The frustration frequently gives rise to highly-degenerate exotic ground-states, including spin glasses, spin ices, spin liquids, topological states, or even complex magnetic orders. [3–6] Materials that realise these frustrated magnetic lattices provide mechanisms to test and refine the predictions of

these increasingly complex theoretical models of the interactions of electrons in solids.

There are two noteworthy families of compounds that contain the frustrated pyrochlore lattice. The main representatives are the $A_2B_2X_6X'$ pyrochlores ($A, B =$ rare earth or transition metals; $X = \text{O}, \text{F}$ and $X' = \text{O}, \text{F}, \text{S}$). [7–10] In this family, both the A and B sites each contain one independent sublattice of corner-sharing tetrahedra. The other family, the AB_2X_4 spinels ($B =$ rare earth, $X = \text{S}, \text{Se}$) only contain a single pyrochlore sublattice on the rare-earth B -site. [11,12] Deviations from the ideal pyrochlore structure can also be found in the so-called “ β -pyrochlores” $AM^{2+}M^{3+}F_6$ ($A^+ = \text{Rb}, \text{Cs}$; $M^{2+} = \text{Mn}, \text{Co}, \text{Ni}$ and $M^{3+} = \text{V}, \text{Cr}, \text{Fe}$) [13] or “breathing pyrochlores” in chromium-based $AA'\text{Cr}_4\text{X}_8$

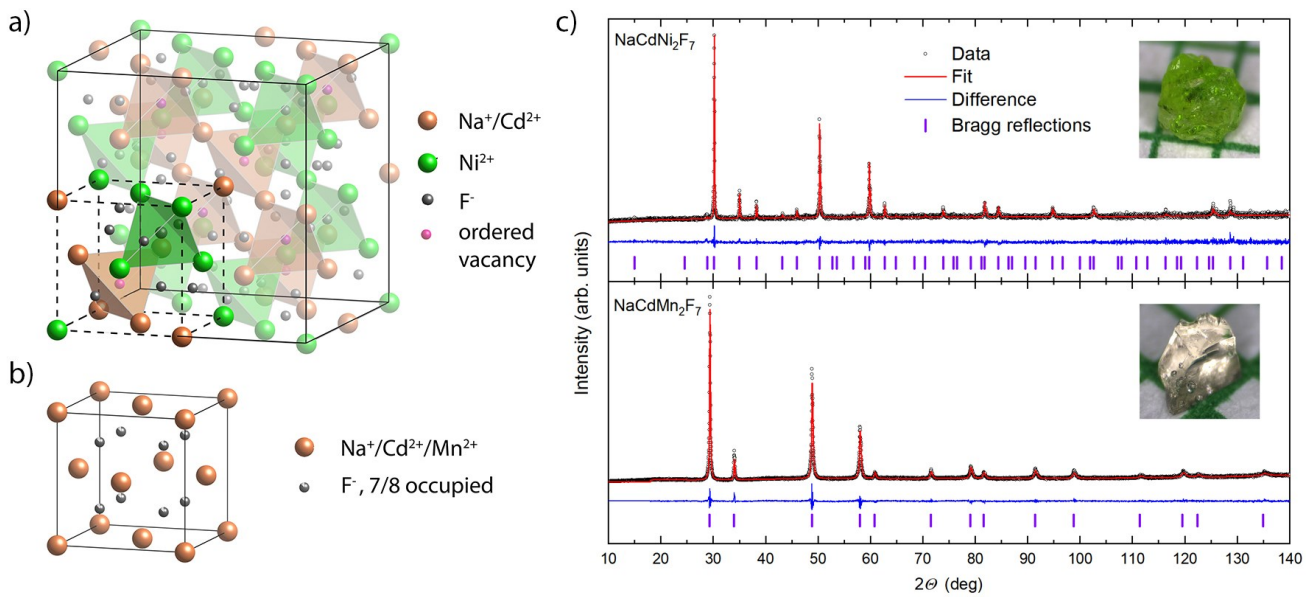


Figure 1. (a) The pyrochlore unit cell of NaCdNi₂F₇, with the (b) disordered defect fluorite cell of NaCdMn₂F₇. The cation ordering and vacancy ordering of the pyrochlore structure leads to a doubling of the cell along each axis. We have highlighted the representative comparison between the two structures as a dashed sub-cell within the pyrochlore structure. Ionic sizes are not-to-scale. (c) Shows powder diffraction data with Rietveld refinement fits and residuals for both compounds, as well as photos of the resulting single-crystal fragments on mm-square paper, as insets.

spinel ($X = O, S, Se$). While the β -pyrochlores contain disordered mixed-valence magnetic ions M^{2+} and M^{3+} on the pyrochlore B -site and vacancies on the A -site, the breathing pyrochlores contain a network of alternating small and large tetrahedra. [14–16]

In the past couple of decades, the rare-earth-based $A_2B_2O_7$ pyrochlore oxides have been extensively investigated due to the availability of large single crystals and the observation of a plethora of exotic magnetic ground-states. [17] These ranged from unconventional spin-glass ($Y_2Mo_2O_7$) [18], to ordered ($Tb_2Sn_2O_7$) and disordered ($Ho_2Ti_2O_7$) spin-ice [19,20], spin-liquid ($Tb_2Ti_2O_7$) [21] or order-by-disorder states ($Er_2Ti_2O_7$). [22] The complex magnetism has been found robust even against structural disorder at the pyrochlore stability boundary, when the size difference between A and B site ions is too small and a defect fluorite structure is instead formed. [23,24]

The variety of properties seen in the $4f$ rare-earth pyrochlores comes about due to the enhanced importance of single-ion anisotropy as a result of a large spin-orbit coupling, as well as interaction with neighbors via crystal-electric-field effects or further-neighbor exchange. The weak dipolar

coupling between the magnetic $4f$ orbitals typically leads to low interaction strengths ($|\theta_{CW}| \sim 10^0 - 10^1$ K), requiring very low temperatures to study the exotic ground-states. Implementing a late $3d$ -metal magnetic ion (from Fe^{2+} to Cu^{2+}) with much greater coupling strengths thanks to superexchange through the more extensive $3d$ orbitals ($|\theta_{CW}| \sim 10^1 - 10^2$ K) would solve this issue, allowing the study of magnetic properties at more accessible temperatures. However, charge balance and pyrochlore structure stability constraints for the $A_2B_2O_7$ oxides hinder this possibility, only allowing the implementation of higher-spin-state transition metals (4+ or 5+) on the pyrochlore B -site. [25]

The family of $A'A''B_2F_7$ pyrochlore fluorides offers a solution. Because of the similar ionic radii of fluorine ($r_{F^-} = 1.33$ Å) and oxygen ($r_{O^{2-}} = 1.4$ Å), as well as similar electronegativities ($X_F = 3.98$ and $X_O = 3.44$), this material family maintains a stable pyrochlore structure by replacing the divalent oxygen (O^{2-}) by a monovalent fluorine (F^{-}). The smaller charge of fluorine then allows for a magnetic $3d$ -metal ion with a low oxidation state (2+) on the pyrochlore B -site. Due to charge balancing, however, there is a necessity for a fully mixed occupancy of the A -site by a monovalent A'^{+} and a divalent A''^{2+} cation, $(A'^{+}_{0.5}A''^{2+}_{0.5})_2B^{2+}_2F^{1-}_7$, yielding

an effective $A^{1.5+}$ oxidation state to maintain the 2:2:7 pyrochlore stoichiometry, ($A^{1.5+}_2B^{2+}_2F^{1-}_7$). This introduces chemical disorder, which in turn locally influences the magnetic exchange pathways due to the ionic size mismatch between the A^{+} and A^{2+} cations. This weak magnetic bond disorder in the Heisenberg pyrochlore antiferromagnet then typically precipitates a frozen spin-glass ground-state. [26,27]

Beyond the initial synthesis and structural report of some polycrystalline $A'A''M_2F_7$ pyrochlore fluorides in 1970 [28], their magnetism has been neglected until the first successful floating-zone growths of large $NaA''M_2F_7$ single crystals (with $A''^{2+} = Ca, Sr, Cd$; and $M^{2+} = Co, Ni, Fe, Mn$). [29–33] All members exhibit strong antiferromagnetic interactions $|\theta_{CW}| \sim 70 - 140$ K with no apparent magnetic transition until $T_f \sim 2 - 4$ K, indicating a sizable frustration with the frustration index $f = \frac{|\theta_{CW}|}{T_f}$ ranging between 19 – 58. In all reported cases, the materials behave as thermal spin liquids until the frustration is quenched by means of spin freezing into a disordered glassy ground-state, selected from the large manifold of degenerate antiferromagnetic states. AC susceptibility measurements suggest a spin-glass ground-state in $NaCaFe_2F_7$, $NaSrFe_2F_7$ and $NaSrMn_2F_7$ [33], in agreement with the ab initio DFT + U + SOC calculations of magnetic and critical properties of $NaSrMn_2F_7$. [34] Inelastic neutron scattering and NMR studies of the $J_{eff} = \frac{1}{2}$ $NaA''Co_2F_7$ ($A'' = Ca, Sr$) suggest a glass-like short-range-ordered state with antiferromagnetic XY-type clusters. [35–37] A recent study of the isostructural $J_{eff} = \frac{1}{2}$ $NaCdCo_2F_7$ showed a positive correlation between the freezing temperature, T_f and the Na^+/A''^{2+} ionic-size-mismatch, comparing with the isostructural $NaA''Co_2F_7$ members ($A'' = Ca, Sr$). [31] In spite of the spin freezing also seen in the $S = 1$ $NaCaNi_2F_7$, persistent spin dynamics down to 75 mK were detected via muon spin relaxation spectroscopy. [38] Inelastic neutron scattering also revealed a continuum of magnetic scattering with low-energy pinch-points, suggesting that $NaCaNi_2F_7$ shows important features of a quantum spin liquid ground-state in the spin-1 antiferromagnetic Heisenberg model on a pyrochlore lattice. [39,40]

In this paper, we report the successful synthesis and structural, magnetic, and thermodynamic characterisation of two new additions to the $A'A''M_2F_7$ fluoride family: $S = 1$ pyrochlore fluoride antiferromagnet $NaCdNi_2F_7$, and $S = 5/2$ defect-fluorite antiferromagnet $NaCdMn_2F_7$.

Experimental

Single crystals of $NaCdNi_2F_7$ and $NaCdMn_2F_7$ were grown by slow crystallization from the melt in platinum crucibles sealed in an argon atmosphere. A stoichiometric mix of dry precursor binary fluorides was prepared and ground inside a glove-box, filled into a platinum crucible, and crimp-sealed in argon to prevent the presence of air and moisture, avoiding possible oxidation. The crucibles were heated inside a box furnace, with the heating protocols programmed to reach 850°C ($NaCdMn_2F_7$) and 950°C ($NaCdNi_2F_7$) at the rate of 2°C/min, dwell there for 3 hours, then slow-cool by 200°C over 7 days and finally rapidly cool to room temperature. This was repeated 4 times, with intermittent grinding to improve homogeneity and ensure a complete reaction. A large multi-grain crystal (~ 0.5 g) of $NaCdMn_2F_7$ was obtained, which could be broken into smaller (~ 30 mg) single-grain pieces. However, only several small ($\sim 1-2$ mg) single-grain crystals of $NaCdNi_2F_7$ could be obtained, while the rest of the reacted material consisted of sintered polycrystalline powder. Single-grain pieces were used for structural solution via single crystal X-ray diffraction, although only $NaCdMn_2F_7$ crystals were big enough to be oriented using a PhotoScience Laue diffractometer to perform directional magnetic and thermodynamic property measurements.

Single-crystal X-ray diffraction experiments were performed at 95 K on a Rigaku SuperNova diffractometer, using a mirror collimated Mo K α ($\lambda = 0.7173$ Å) radiation from a microfocus sealed tube, and an Atlas S2 CCD detector. Diffraction data were integrated using CrysAlis Pro [41] with an empirical absorption correction using spherical harmonics ($NaCdMn_2F_7$), and an empirical absorption correction using spherical harmonics combined with a numeric absorption correction based on Gaussian integration over a multifaceted crystal model ($NaCdNi_2F_7$). The structure was solved by charge flipping using the program Superflip [42] and refined by full-matrix least squares on F^2 in Jana2020. [43] Structural graphics were created using Jana2020 and Vesta. [44]

To confirm that the single crystal structure solutions were representative of the bulk of the sample, a small number of individual grains were selected, crushed into a fine powder and analyzed by Powder X-Ray Diffraction (PXRD) at room temperature ($T = 300$ K) using a Bruker D8 Advance diffractometer with Cu K α radiation ($\lambda = 1.5418$ Å). Structural Rietveld refinement was performed using Topas Academic V6. [45]

Temperature and field-dependent magnetization measurements on oriented crystals of NaCdMn₂F₇ and polycrystalline NaCdNi₂F₇ were performed in a Quantum Design Magnetic Property Measurement System (model MPMS-XL 7T), using the DC extraction method (NaCdMn₂F₇) as well as the reciprocating sample option (RSO, NaCdNi₂F₇). Spin dynamics were probed by temperature and frequency dependent AC susceptibility measurements using the ACMS II option in a Quantum Design Physical Property Measurement System (PPMS). Specific heat between 1.8 – 300 K was measured inside the PPMS using the relaxation method, with the addition of a ³He insert for low-temperature measurements down to 0.4 K. A Quantum Design heat capacity puck with a non-magnetic sapphire stage was used, with Apiezon-N grease for mounting the crystal. Measurement of a non-magnetic analogue NaCdZn₂F₇ was used in the subtraction of the phonon contribution to the specific heat of NaCdNi₂F₇ and NaCdMn₂F₇ to estimate the magnetic specific heat.

Results and Discussion

Structure analysis

Single-crystal experimental results follow in Tables 1-3.

The crystal structure of NaCdNi₂F₇ obtained by SCXRD at 95 K is cubic, space group *Fd-3m* (#227), *Z* = 8, and with unit cell parameter $a_{\text{Ni}} = 10.2245(10)$ Å. This is consistent with the expected pyrochlore structure, shown in Figure 1 (a). An initial model with Na and Cd sharing the 16*d* site with a Na:Cd ratio of 1:1 gave $R_{\text{obs}} = 3.51\%$ and $GOF_{\text{obs}} = 4.49\%$. However, refined F2 and Na:Cd occupancies, whilst maintaining a full site occupancy of the 16*d* site, lowered the residue values to $R_{\text{obs}} = 1.83\%$ and $GOF_{\text{obs}} = 1.19\%$. This gives the final chemical composition Na_{0.892}Cd_{1.108}Ni₂F_{6.982}. An attempt at refining only the Na/Cd occupancy site gave a chemical composition of Na_{0.894}Cd_{1.106}Ni₂F₇, making almost no difference in the residue values, slightly increasing the GOF_{obs} from 1.19% to 1.23%. The error on the F2 site occupancy is in the third position [0.982(9)], while the Na/Cd occupancies variations are within the error [0.4459(19) for Na and 0.5541(19) for Cd], which suggests that the refinement is much less sensitive to the light element F2 site occupancy. Charge balancing arguments, however, would expect that an increase in the Cd²⁺ cation occupancy above the ideal 1:1:2:7 Na:Cd:Ni:F ratios, and at the expense of the Na⁺ occupancy, would require an increase in the total F⁻ anion stoichiometry. We saw no evidence for additional F⁻ sites within the structure to charge balance the slight excess of the Cd²⁺

cation, but expect that the minor occupation of interstitial or vacancy sites necessary for this are below the resolution of our measurements.

The crystal structure of NaCdMn₂F₇ obtained by SCXRD at 95 K is cubic, space group *Fm-3m* (#225), *Z* = 1, and with unit cell parameter $a_{\text{Mn}} = 5.2461(5)$ Å. The cation site (4*a*) is shared by Na⁺, Cd²⁺ and Mn²⁺ in a ¼ : ¼ : ½ ratio, remaining fully disordered, as seen in Figure 1 (b). The ADPs of Na/Cd/Mn were kept fixed to be the same for all atoms sharing the site, and occupancies were fixed to the ideal ratios. The occupancy of fluorine on the 8*c* site was constrained to 7/8 to retain the expected NaCdMn₂F₇ stoichiometry, which lead to a residue value of $R_{\text{obs}} = 1.97\%$ and $GOF_{\text{obs}} = 1.97\%$. This solution is consistent with the defect-fluorite structure, where F is known to have a disordered vacancy, decreasing its occupancy from 8 to 7 atoms per unit cell, and analogous to oxides of the same type. [24,46] In contrast, assuming full F site occupancy (NaCdMn₂F₈) lead the refinement to significantly worse residue values $R_{\text{obs}} = 2.87\%$ and $GOF_{\text{obs}} = 3.90\%$, as expected from the initial fluorine content in the stoichiometric mix of precursor binary fluorides.

The powder X-ray diffraction patterns of NaCdNi₂F₇ and NaCdMn₂F₇ confirm the expected pyrochlore (SG: *Fd-3m*, #227:2) and defect-fluorite (SG: *Fm-3m*, #225) structures, respectively. The refined lattice parameters, $a_{\text{Ni}} = 10.257(1)$ Å and $a_{\text{Mn}} = 5.271(1)$ Å, are in line with previous reports [28] and consistent with our SCXRD results (taken at 95 K) after considering thermal expansion.

Comparing the PXRD patterns of the two samples, seen in Figure 1 (c), highlights the structural differences, where superstructure reflections stemming from the cation ordering and fluoride ion vacancy ordering of the pyrochlore lattice are clearly present in NaCdNi₂F₇ *but absent in* NaCdMn₂F₇. The reason behind NaCdMn₂F₇ crystallizing in the defect-fluorite structure instead of the pyrochlore structure lies in the large ionic radius of Mn²⁺, which in the high-spin state and a six-fold coordination amounts to $r_{\text{Mn}^{2+}} = 0.83$ Å. [47] The simplest and most-widely used descriptor of the A₂B₂O₇ pyrochlore structure stability region is given by the ratio of the A-site and B-site ionic radii $RR = R_A/R_B$, where a stable pyrochlore structure on the oxide series is expected for $RR \in [1.46, 1.80]$. [8] Using 8-fold-coordinated Shannon radii [47] for the average ionic radius of the A-site shared by Na⁺ (1.18 Å) and Cd²⁺ (1.10 Å), gives $R_A = 1.14$ Å and $RR = 1.37$, outside the lower bound for

Table 1: Single crystal experimental results and structural refinement of NaCdMn₂F₇ and NaCdNi₂F₇

Crystal data	Mn	Ni
Chemical formula	NaCdMn ₂ F ₇	Na _{0.892} Cd _{1.108} Ni ₂ F _{6.982}
Crystal system, Space group	cubic, Fm-3m (#225)	cubic, Fd-3m (#227): setting 2
Temperature (K)	95	95
<i>a</i> (Å)	5.2461(5)	10.2245(10)
Crystal size (mm)	0.119 x 0.087 x 0.017	0.22 x 0.16 x 0.105
Color, shape	light yellow, plate	lime green, irregular
<i>V</i> (Å ³), <i>Z</i>	144.38(2), 1	1068.88(18), 8
λ (MoK α) (Å)	0.710	
μ (mm ⁻¹)	8.101	11.483
ϑ Range (°)	6.74, 37.29	3.45, 29.68
<i>F</i> (000) / <i>D_x</i> (Mg.m ⁻³)	172/4.3504	1455, 4.9102
	-8 ≤ <i>h</i> ≤ 8	-14 ≤ <i>h</i> ≤ 13
Index ranges	-8 ≤ <i>k</i> ≤ 8	-13 ≤ <i>k</i> ≤ 13
	-8 ≤ <i>l</i> ≤ 8	-14 ≤ <i>l</i> ≤ 14
independent reflections	35	95
measured reflections	1189	4405
Observed data (<i>I</i> > 3σ(<i>I</i>))	35	74
Refinement method	Refinement on <i>F</i> ²	
<i>R</i> _{int}	0.0447	0.0949
Diffractometer	SuperNova, Dual, Mo at home/near, AtlasS2	
	Multi-scan	
Absorption correction	CrysAlisPro 1.171.41.117a (Rigaku Oxford Diffraction, 2021) Empirical absorption correction using spherical harmonics, implemented in SCALE3 ABSPACK scaling algorithm.	
Structure solution	Charge flipping	
Refinement Software	Jana2020	
<i>R</i> [<i>F</i> ² > 3σ(<i>F</i> ²)], <i>wR</i> ₂ (<i>F</i> ²), GOF	0.0197, 0.0775, 1.9723	0.0183, 0.0534, 1.1396
No. of Parameters, restraints, constraints	4, 0, 3	13, 0, 2
$\Delta\rho_{\max}$, $\Delta\rho_{\min}$ (e Å ⁻³)	0.48, -0.62	0.34, -0.49
CCDC Number	2389766	2389764

Table 2: Atomic positions and anisotropic thermal displacement parameters of NaCdMn₂F₇

NaCdMn ₂ F ₇													
Atom	Site	x	y	z	Occ.	Site sym.	U_{ij} ($\times 10^4 \text{ \AA}^2$)						
							U_{11}	U_{22}	U_{33}	U_{12}	U_{13}	U_{23}	U_{ani}
Na	4a	0	0	0	¼	m-3m	232(6)	232(6)	232(6)	0	0	0	232(3)
Cd	4a	0	0	0	¼	m-3m	232(6)	232(6)	232(6)	0	0	0	232(3)
Mn	4a	0	0	0	½	m-3m	232(6)	232(6)	232(6)	0	0	0	232(3)
F	8c	¼	¼	¼	¾	-43m	560(2)	560(2)	560(2)	0	0	0	558(14)

Table 3: Atomic positions and anisotropic thermal displacement parameters of NaCdNi₂F₇

Na _{0.892} Cd _{1.108} Ni ₂ F _{6.982}													
Atom	Site	x	y	z	Occ.	Site sym.	U_{ij} ($\times 10^4 \text{ \AA}^2$)						
							U_{11}	U_{22}	U_{33}	U_{12}	U_{13}	U_{23}	U_{ani}
Na	16d	½	½	½	0.4462(17)	-.3m	93(4)	93(4)	93(4)	-7(9)	-7(9)	-7(9)	93(2)
Cd	16d	½	½	½	0.5538(17)	-.3m	93(4)	93(4)	93(4)	-7(9)	-7(9)	-7(9)	93(2)
Ni	16c	0	0	0	1	-.3m	56(4)	56(4)	56(4)	0(1)	0(1)	0(1)	56(2)
F1	48f	0.33201(15)	⅙	⅙	1	2.mm	105(5)	131(9)	105(5)	0	33(5)	0	113(4)
F2	8b	⅙	⅙	⅙	0.982(9)	-43m	125(9)	125(9)	125(9)	0	0	0	125(5)

a stable pyrochlore structure. This results in full cation disorder, as well as disorder of the vacancy of the 7/8th occupied fluoride site in the fluorite structure. In contrast, $RR = 1.65$ in NaCdNi₂F₇ lies well in the middle of the stability region, resulting in a stable pyrochlore structure.

Magnetic susceptibility

NaCdNi₂F₇ DC susceptibility

Temperature and field-dependent DC magnetization $M(T,H)$ measurements were conducted on polycrystalline NaCdNi₂F₇. The temperature dependence of magnetization $M(T)$ in a constant field of $\mu_0H = 2$ T is shown as $\chi(T)$ and $\chi(T)^{-1}$ for NaCdNi₂F₇ in Figure 2. The field-dependent magnetization measured at 2 K is presented in the lower inset of Figure 2 and shows a linear response up to $\mu_0H = 7$ T, without hysteresis effects, justifying the consideration of the magnetisation data as DC susceptibility as $\chi(T) = M(T)/H$. At $\mu_0H = 7$ T the moment remains far below the expected saturated moment (2 μ_B) for an orbitally quenched moment on $S = 1$ Ni²⁺. A Curie-Weiss fitting was performed in the 100 – 300 K range, resulting in a Curie-Weiss

temperature $\theta_{CW} = -91.2(5)$ K and the effective moment $\mu_{eff} = 3.15(1)$ μ_B/Ni^{2+} . In spite of the strong antiferromagnetic interactions evidenced by the large negative Curie-Weiss temperature, no features in the susceptibility are seen until cooling below $T_f = 3.2$ K. The upper inset of Figure 2 shows a low-field measurement of susceptibility, where a sharp cusp indicates a magnetic transition that yields a significant Ramirez frustration index of $f = -\theta_{CW}/T_f = 28.5$. [1] A bifurcation of the ZFC/FC data at the transition is characteristic of either magnetic order or spin-glass freezing, as seen with the spin-glass state of the previously-reported pyrochlore fluorides. [29–33] The spin-glass nature of this transition in NaCdNi₂F₇ is confirmed by AC susceptibility and specific heat measurements, discussed later. From the electron configuration of $S = 1$ Ni²⁺ ($t_{2g}^6e_g^2$) in a six-fold-coordinated octahedral environment, where the three t_{2g} shells are fully occupied and the two e_g shells are singly occupied, one would expect a quenching of the orbital moment, leading to a spin-only effective moment of 2.83 μ_B/Ni^{2+} . The larger effective moment extracted from the Curie-Weiss fit, however, suggests a small but non-zero orbital contribution, likely coming about from the crystal field effects from the trigonally-distorted NiF₆ octahedra. This effect, although stronger, was also seen in the

isostructural analogue $\text{NaCaNi}_2\text{F}_7$ ($\mu_{\text{eff}} = 3.7 \mu_{\text{B}}$). [32] Table 4 shows a compilation of the magnetic properties for all members of this transition metal fluoride family.

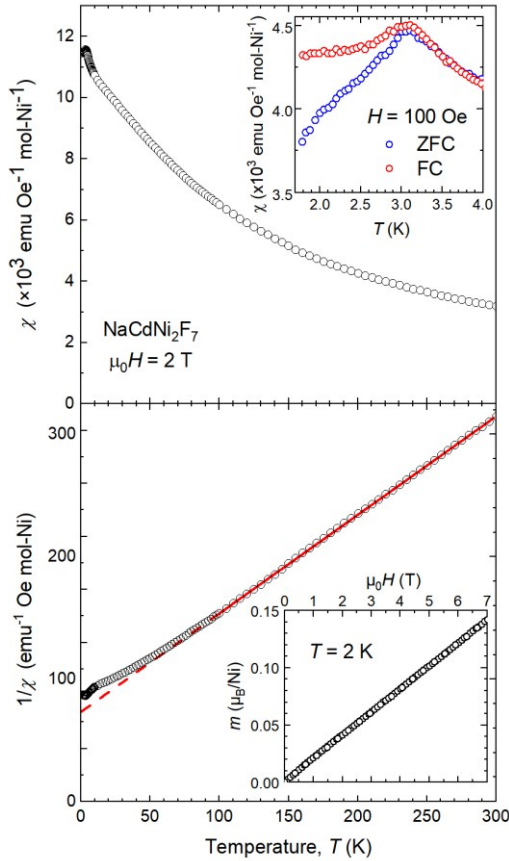


Figure 2. Temperature dependent magnetic susceptibility (upper) and inverse susceptibility (lower) data for $\text{NaCdNi}_2\text{F}_7$. The red solid (dashed) line is the Curie-Weiss fit (extrapolation). Upper inset is a low-field measurement, indicating the ZFC-FC history dependence below $T_f = 3.2$ K, whilst the lower inset highlights the linear magnetisation that is seen at all temperatures.

$\text{NaCdMn}_2\text{F}_7$ DC susceptibility

The magnetic susceptibility and inverse susceptibility of $\text{NaCdMn}_2\text{F}_7$, measured along $H \parallel [100]$, $[110]$ and $[111]$ directions in an $H = 2000$ Oe field are shown in Figure 3. The isothermal magnetization $M(H)$ measured at 2 K, shown in the lower inset of Figure 3, displays a subtle curvature up to $\mu_0 H = 7$ T, but is linear in the vicinity of $H = 2000$ Oe and shows no hysteresis upon decreasing the field, again supporting our interpretation of DC susceptibility as $\chi = M/H$. Due to the strong magnetic frustration, the magnetization at 7 T reaches only around 20% of the saturated value expected for

an orbitally quenched $S = 5/2$ Mn^{2+} ion ($5 \mu_{\text{B}}$), which is typical in compounds of 3d transition metal ions as a result of the crystal-field splitting. The $M(H)$ and $\chi(T)$ curves overlay in all high-symmetry directions, suggesting a Heisenberg (isotropic) nature of this defect-fluorite antiferromagnet. The inverse susceptibility data along $[111]$ were fitted to the Curie-Weiss law in the 100 – 300 K range, yielding a Curie-Weiss temperature of $\theta_{\text{CW}} = -42.4(4)$ K and an effective moment of $\mu_{\text{eff}} = 5.88(2) \mu_{\text{B}}/\text{Mn}^{2+}$. The negative Curie-Weiss temperature confirms dominant antiferromagnetic interactions, while the magnitude is ~ 2 times lower than that observed in the pyrochlore analogue $\text{NaSrMn}_2\text{F}_7$. [33] The crossover from ordered pyrochlore structure to disordered defect-fluorite is expected to result in significant changes to the magnetic behaviour. The magnetic ions no

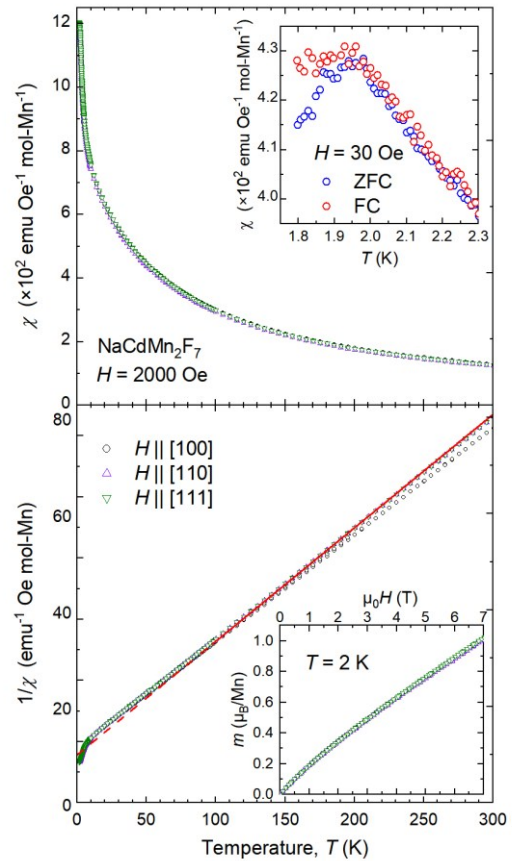


Figure 3. Temperature dependent magnetic susceptibility (upper) and inverse susceptibility (lower) data for $\text{NaCdMn}_2\text{F}_7$ along selected high-symmetry crystal directions. The solid (dashed) line is the Curie-Weiss fit (extrapolation). Upper inset is a low-field measurement, indicating the ZFC-FC history dependence below $T_f = 2.0$ K, whilst the lower inset highlights the slight curvature of the magnetisation at low temperature.

Table 4: Magnetic properties comparison of previously studied AA'B₂F₇ pyrochlore (defect-fluorite) antiferromagnets.

Compound	Space Group	S	μ_{eff} (μ_B/M^{2+})	θ_{CW} (K)	T_f (K)	$f = \frac{-\theta_{\text{CW}}}{T_f}$	References
NaCdNi ₂ F ₇	$Fd\bar{3}m$	1	3.15(1)	-91.2(5)	3.2	28.5	This work
NaCaNi ₂ F ₇	$Fd\bar{3}m$	1	3.7(1)	-129(1)	3.6	36	[32]
NaCdMn ₂ F ₇	$Fm\bar{3}m$	$\frac{5}{2}$	5.88(2)	-42.4(4)	2.0	21	This work
NaSrMn ₂ F ₇	$Fd\bar{3}m$	$\frac{5}{2}$	6.25	-89.72	2.5	36	[33]
NaCdCo ₂ F ₇	$Fd\bar{3}m$	$\frac{3}{2}$ ($J_{\text{eff}} = \frac{1}{2}$)	5.4(1)	-108(1)	4.0	27	[31]
NaCaCo ₂ F ₇	$Fd\bar{3}m$	$\frac{3}{2}$ ($J_{\text{eff}} = \frac{1}{2}$)	6.1(1)	-139(1)	2.4	58	[29]
NaSrCo ₂ F ₇	$Fd\bar{3}m$	$\frac{3}{2}$ ($J_{\text{eff}} = \frac{1}{2}$)	5.9(1)	-127(1)	3.0	42	[30]
NaCaFe ₂ F ₇	$Fd\bar{3}m$	2	5.61	-72.79	3.9	19	[33]
NaSrFe ₂ F ₇	$Fd\bar{3}m$	2	5.94	-98.12	3.7	26.5	[33]

longer reside on a pyrochlore lattice, but instead now sit on an FCC lattice with significant (50 %) dilution. The FCC lattice is also considered geometrically frustrated, however, to a much lesser degree than the pyrochlore lattice due to a reduced number of soft modes in the correlated paramagnetic state. [48] The local disorder that the significant dilution brings about results in a weaker but still sizable mean-field interaction. Despite these strong exchange interactions, no magnetic transition is apparent down to approximately $T_f = 2.0$ K, where a rounded cusp in $\chi(T)$ begins to appear, yielding a frustration index of $f = 21.2$. Due to the close proximity of the transition to the MPMS's base temperature (1.8 K), only a weak ZFC/FC splitting in 30 Oe field could be seen at the transition (upper inset of Figure 3). In the octahedral crystal field environment, the $3d^5$ Mn²⁺ ion usually takes the high-spin ($t_{2g}^3e_g^2$) electronic configuration, where each of the individual t_{2g} ($|xy\rangle$, $|xz\rangle$, $|yz\rangle$) and e_g ($|x^2-y^2\rangle$, $|z^2\rangle$) orbitals is singly occupied. The spin-only effective moment expected for a free $S = 5/2$ Mn²⁺ ion (ground term ${}^6S_{5/2}$, $L = 0$) is $5.92 \mu_B$, which is in line with the magnitude of the measured effective moment. This result is in contrast with the effective moment seen in the NaSrMn₂F₇ pyrochlore, where some orbital contribution was seen due to crystal field effects ($6.25 \mu_B/\text{Mn}^{2+}$), seen in Table 4. [33]

To directly compare the susceptibility data of different magnetic materials, one can rearrange the Curie-Weiss law into a normalized dimensionless form $C/\chi|\theta_{\text{CW}}| = T/|\theta_{\text{CW}}| + 1$. Here, the susceptibility is scaled by the effective moment ($C \sim \mu_{\text{eff}}^2$) as well as the mean-field interaction strength ($\theta_{\text{CW}} \sim J$), and is plotted against the normalized temperature $T/|\theta_{\text{CW}}|$. Considering an ideal unfrustrated antiferromagnet,

the normalized high-temperature susceptibility would follow the line $y = x + 1$, with the gradient as well as y -intercept both equal to one. A long-range ordering transition would be expected to be seen as a cusp in the susceptibility in the vicinity of $T_N/|\theta_{\text{CW}}| \sim 1$. The magnetic frustration, however, pushes the magnetic transition to much lower temperature than the mean-field interaction strength $T_f/|\theta_{\text{CW}}| \ll 1$. [29–33] The positive or negative deviations from the ideal Curie-Weiss behaviour signify the onset of enhanced antiferromagnetic or ferromagnetic short-range correlations, respectively.

In Figure 4, we compare the NaCdMn₂F₇ and NaCdNi₂F₇ Curie-Weiss data, including the recently-studied NaCdCo₂F₇ [31]. All three materials follow the ideal Curie-Weiss behaviour very closely at high temperatures ($T_f/|\theta_{\text{CW}}| \geq 1$). However, significant deviations begin to appear as we approach T_f . NaCdMn₂F₇ starts to positively deviate from the ideal Curie-Weiss line below $\sim 3.5 T/|\theta_{\text{CW}}|$ as it develops enhanced antiferromagnetic correlations. As we approach the spin-freezing transition, however, significant ferromagnetic fluctuations begin to develop below $\sim 0.1 T/|\theta_{\text{CW}}|$. NaCdNi₂F₇ follows the ideal Curie-Weiss behaviour down to $\sim 1 T/|\theta_{\text{CW}}|$, where antiferromagnetic fluctuations begin to appear as increasing positive deviations from the ideal line approaching T_f from above. For comparison, NaCdCo₂F₇ appears to follow the ideal Curie-Weiss form down to an extremely low temperature of $\sim 0.06 T/|\theta_{\text{CW}}|$ and only deviates ferromagnetically below this normalized temperature as it approaches the freezing transition.

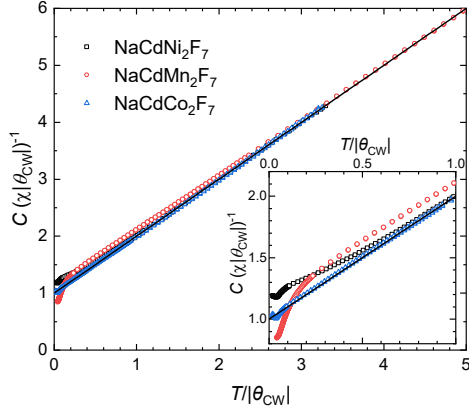


Figure 4. Rearranged dimensionless Curie-Weiss data for the known NaCdM_2F_7 ($M = \text{Ni}, \text{Mn}, \text{Co}$) compounds. The solid line at $C/(\chi|\theta_{\text{CW}}|) = T/|\theta_{\text{CW}}| + 1$ represents ideal Curie-Weiss behaviour.

AC susceptibility

The spin dynamics of the underlying freezing transitions were probed by AC susceptibility measurements using the ACMS II option for the PPMS. Samples were cooled in zero field and the response to an alternating field with a $H_{\text{AC}} = 5$ Oe amplitude was recorded. The frequency ν of the AC field was varied between 100 and 10 000 Hz. The temperature scans of the real part of AC susceptibility, χ' , are plotted for each frequency in Figure 5, for both $\text{NaCdMn}_2\text{F}_7$ and $\text{NaCdNi}_2\text{F}_7$. In both materials, we see a systematic shift of the freezing transition T_f , taken as the maximum of the χ' cusp, to higher temperatures with increasing AC field frequency. This is an archetypal feature of a spin-glass transition, and in conjunction with the ZFC/FC splitting seen at the transition in DC susceptibility, this provides good evidence for a spin-glass ground-state in these materials. A dimensionless parameter quantifying the relative shift of T_f per decade of frequency, $\delta T_f = \Delta T_f / (T_f \Delta \log_{10} \nu)$ was proposed by Mydosh [49] to compare between the various classes of spin-glass-like materials. The extracted values are $\delta T_f = 0.018(1)$ and $0.033(3)$ for $\text{NaCdMn}_2\text{F}_7$ and $\text{NaCdNi}_2\text{F}_7$, respectively, and are in line with the order of magnitude expected for insulating spin-glasses, as was also seen in the previously-reported pyrochlore fluorides $\text{NaCdCo}_2\text{F}_7$ (0.010), $\text{NaCaNi}_2\text{F}_7$ (0.024), $\text{NaSrCo}_2\text{F}_7$ (0.027) and $\text{NaCaCo}_2\text{F}_7$ (0.029). [29–33] The dynamics of the spin-freezing process can be further modelled by the empirical Vogel-Fulcher law: $\nu = \nu_0 \exp\left(-\frac{E_a}{k_B(T_f - T_0)}\right)$. This model assumes interacting clusters of spins with the intrinsic relaxation time $\tau_0 = \nu_0^{-1}$, where an activation energy E_a is needed to trigger a freezing transition into a static disordered state. Here, the *ideal glass*

temperature, T_0 , is taken as the extrapolated freezing temperature at zero frequency and is usually interpreted as an estimate of the inter-cluster interaction strength. One can extract the parameters from a linear fit on the rearranged form of the Vogel-Fulcher law, expressing the frequency-dependence of the freezing temperature $T_f = T_0 - \frac{E_a}{k_B \ln(\tau_0 \nu)}$. Due to a limited experimental frequency range, however, it is physically unreasonable to fit all three parameters independently. Hence, the intrinsic relaxation time is usually fixed to a value typical for insulating spin-glasses, $\tau_0 = 10^{-12}$ s. The extraction of parameters after fixing τ_0 then yields $E_a = 1.6(2)$ meV and $T_0 = 2.4(1)$ K for $\text{NaCdNi}_2\text{F}_7$; and $E_a = 0.64(2)$ meV and $T_0 = 1.72(1)$ K for $\text{NaCdMn}_2\text{F}_7$, summarised in Table 5. In both cases,

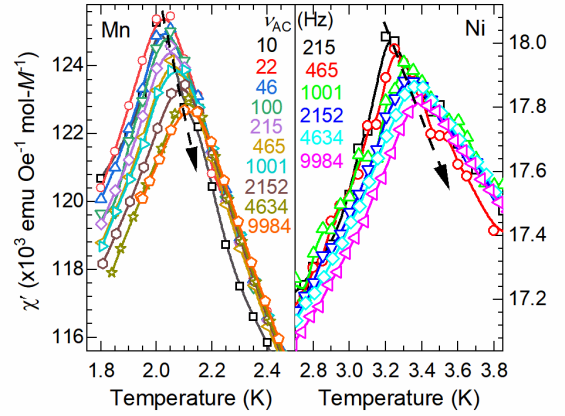


Figure 5. AC-susceptibility data, χ' , for (left) $\text{NaCdMn}_2\text{F}_7$, and (right) $\text{NaCdNi}_2\text{F}_7$. The arrows highlight the shift to higher temperatures of the spin-glass freezing peak with increasing temperature.

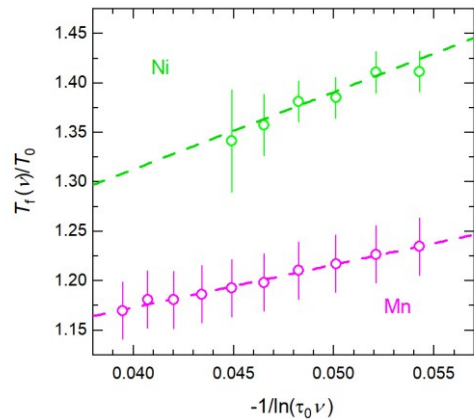


Figure 6. Frequency-dependent shift of the spin-glass freezing transition, normalised to the zero-frequency freezing temperature for $\text{NaCdNi}_2\text{F}_7$ and $\text{NaCdMn}_2\text{F}_7$.

Table 5: Fitted ACMS parameters using the Vogel-Fulcher model and the theory of dynamical scaling. Comparison of our data with the previously-studied AA'B₂F₇ pyrochlore fluorides. *Values were not reported explicitly in [33], but instead were extracted from the Figure 8 digitized. **Dynamical scaling was not reported in [31], but the data were revisited and reanalyzed.

Compound	Fit of $T_f(\nu)$ vs. $\log(\nu)$		Vogel-Fulcher analysis		Dynamical scaling		References
	δT_f	T_0 (K)	T_0 (K)	E_a [meV]	τ_0 (s)	$z\nu'$	
NaCdNi ₂ F ₇	0.033(3)	2.98(4)	2.4(1)	1.6(2)	$3.3(2) \times 10^{-10}$	6.6(8)	This work
NaCaNi ₂ F ₇	0.024	----	3.0(1)	1.4(2)	----	----	[32]
NaCdMn ₂ F ₇	0.018(1)	1.97(1)	1.72(1)	0.64(2)	$1.6(1) \times 10^{-10}$	5.3(3)	This work
NaSrMn ₂ F ₇	*0.018(2)	----	2.2(7)	0.83(4)	----	----	[33]
NaCdCo ₂ F ₇	0.010(1)	**3.91(1)	3.7(1)	0.64(6)	**5.3(2) $\times 10^{-10}$	**4.1(4)	[31]
NaCaCo ₂ F ₇	0.029	----	2.17	1.0	----	----	[29]
NaSrCo ₂ F ₇	0.027	----	2.6(1)	1.3(1)	----	----	[30]
NaCaFe ₂ F ₇	*0.051(3)	----	2.8(4)	2.9(4)	----	----	[33]
NaSrFe ₂ F ₇	*0.057(3)	----	2.7(2)	2.8(1)	----	----	[33]

the fitted ideal glass temperature is lower than that seen as the maximum of the cusp in DC susceptibility. For comparison, values found for NaCaNi₂F₇ and NaSrMn₂F₇ were $E_a = 1.4(2)$ meV and $0.83(4)$ meV; and $T_0 = 3.0(1)$ K and $2.2(7)$ K, respectively. [32,33] In Figure 6, we directly compare our fits, with the y-axis normalized by the respective ideal glass temperatures, T_0 .

Another approach to model the relaxation dynamics during the spin-freezing transition is to use the results of the standard theory of dynamical scaling near T_f , which gives the power-law divergence $\tau = \tau_0 \left(\frac{T_f - T_{SG}}{T_{SG}} \right)^{-z\nu'}$. [49,50] Here, $T_f = T_f(\nu)$ is the frequency-dependent maximum of the χ' cusp, T_{SG} should correspond to the extrapolated value of T_f as $\nu \rightarrow 0$, z is the dynamical critical exponent, and ν' is the critical exponent of the correlation length. In spin glasses, the values of the product $z\nu'$ typically lie between 4 and 12, whereas in conventional phase transitions $z\nu'$ is around 2. [49] These parameters can be extracted after rearranging the power-law divergence as $\ln(\tau) = \ln(\tau_0) - z\nu' \ln \left(\frac{T_f - T_{SG}}{T_{SG}} \right)$ and performing a linear fit of $\ln(\tau)$ versus $\ln \left(\frac{T_f - T_{SG}}{T_{SG}} \right)$, where $\tau = \nu^{-1}$. The critical exponents and intrinsic relaxation times extracted from the fits are $z\nu' = 6.8(8)$ and $5.3(3)$; and $\tau_0 = 3.3(2) \times 10^{-10}$ s and $1.6(1) \times 10^{-10}$ s for NaCdNi₂F₇ and

NaCdMn₂F₇, respectively. Here, T_{SG} was taken as the linear extrapolation of $T_f(\nu)$ vs. $\ln(\nu)$ to zero frequency – $2.98(4)$ K and $1.97(1)$ K for NaCdNi₂F₇ and NaCdMn₂F₇, respectively. Both critical exponents lie well in the $z\nu' \in [4, 12]$ region expected for spin-glasses. However, the extracted relaxation times suggest two orders of magnitude slower relaxation dynamics than the estimated value $\tau_0 = 10^{-12}$ s used in the Vogel-Fulcher fits as a fixed parameter.

Specific heat

The magnetic ground-states of NaCdNi₂F₇ and NaCdMn₂F₇ were further probed by specific heat measurements. For the estimation of phonon contribution to the specific heat, allowing a subtraction to separate the magnetic component, a non-magnetic analogue NaCdZn₂F₇ was used (after slight individual scaling necessary due to differing unit cell volume). The temperature dependences of the specific heat are shown in Figure 7. Noting that the studied materials are insulating, no additional contribution to the specific heat from conducting electrons is present, allowing us to estimate the magnetic specific heat as $C_{mag} = C_p - C_{lattice} \approx C_{p[NaCdM2F7]} - C_{p[NaCdZn2F7]}$ ($M = Ni, Mn$). In both materials, we see a broad peak in the magnetic specific heat below 20 K, a typical feature seen in spin-glass materials as spin-correlations build. A sharp peak can be seen

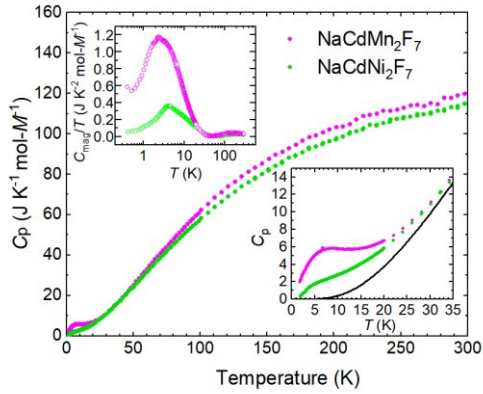


Figure 7. Heat capacity vs. temperature for NaCdMn₂F₇ and NaCdNi₂F₇. The solid line of the lower inset indicates the heat capacity of the non-magnetic analogue NaCdZn₂F₇. The upper inset shows the extracted C_{mag}/T after subtraction of the phonon contribution.

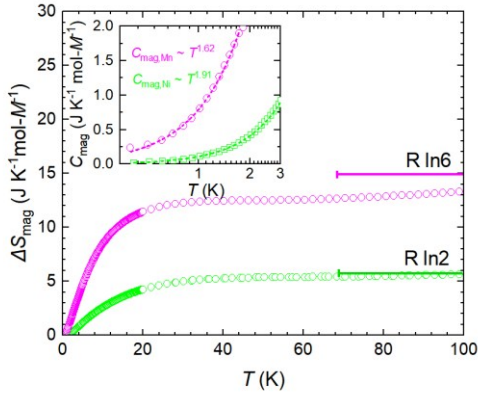


Figure 8. The extracted magnetic entropy vs. temperature for NaCdMn₂F₇ and NaCdNi₂F₇, showing saturation above ~ 30 K. The inset shows the low-temperature magnetic contribution to specific heat, with fits to power-law behaviour indicated by the dashed lines.

roughly at T_f on the C_{mag}/T vs. T scale, with no additional broadening after applying an external field up to 9 T. Below T_f , the materials exhibit a power-law decay of the magnetic specific heat, which was fitted in the $T < T_f$ region to a simple power function in the form $C_{\text{mag}} = AT^\alpha$. The extracted parameters are $A = 0.110(1)$ J mol-Ni⁻¹ K^{-1- α} and $\alpha = 1.91(1)$ for NaCdNi₂F₇, as well as $A = 0.79(1)$ mol-Mn⁻¹ K^{-1- α} and $\alpha = 1.62(3)$ for NaCdMn₂F₇. Usually, a linear dependence of the magnetic specific heat ($\alpha = 1$) is expected below T_f in canonical (metallic) spin-glasses, arising from a statistical distribution of localized tunnelling levels linear in energy. [51] In the case of insulating spin-glass materials, a power-law dependence is

usually observed, with the exponent typically close to $\alpha \sim 2$, as was seen in the isostructural analog NaCaNi₂F₇ ($\alpha = 2.2$). [39]

The magnetic entropy, $\Delta S_{\text{mag}}(T)$ was extracted by integration of the C_{mag}/T vs. T data and is shown in Figure 8. In both materials, the magnetic entropy saturates at about 50 K. In NaCdMn₂F₇ the saturation value reaches about 85% of the high-temperature Heisenberg limit expected for an $S = 5/2$ Mn²⁺ ion, $S_{\text{mag}} = R \ln(2S+1) = R \ln(6)$. In contrast, the magnetic entropy of NaSrMn₂F₇ was seen to begin saturating higher than $R \ln(6)$ at 70 K. [33] In NaCdNi₂F₇, the magnetic entropy surprisingly saturates at a very low value of $R \ln(2)$, significantly short of the Heisenberg value of $R \ln(3)$ expected for a $S = 1$ Ni²⁺ ion. Both materials thus suggest a large residual entropy at 0.4 K, indicating continued dynamics at low temperature. This was also seen in NaCaNi₂F₇, where the magnetic entropy extracted from specific heat measured down to 1.8 K also saturated at $R \ln(2)$ [32], although employing a dilution fridge down to 100 mK later suggested a saturation of magnetic entropy at about 84% of $R \ln(3)$, with residual entropy of 0.176R at 100 mK. [39]

Conclusions

We report a successful single-crystal growth of the $S = 1$ pyrochlore antiferromagnet NaCdNi₂F₇ and the $S = 5/2$ defect-fluorite antiferromagnet NaCdMn₂F₇, on which we performed structural, magnetic and thermodynamic studies.

Structural analysis confirms the expected pyrochlore structure of NaCdNi₂F₇ (cubic, SG: $Fd\bar{3}m$, $a = 10.2245(10)$ Å), with SCXRD refinement leading to a formula Na_{0.892}Cd_{1.108}Ni₂F_{6.982}. The A-site cations (Na/Cd) are fully disordered, with a $\sim 11\%$ preference for Na⁺ deficiency and Cd²⁺ excess. NaCdMn₂F₇ crystallizes in the defect-fluorite structure (cubic, SG: $Fm\bar{3}m$, $a = 5.2461(5)$ Å), as the Mn²⁺ ion is too similar to the average A-site ionic size to drive the cationic site order of the stable pyrochlore structure. For NaCdMn₂F₇, the ratio of A-site and B-site ionic radii $RR = R_A/R_B = 1.37$ lies below the lower boundary for pyrochlore structure stability [8]. Instead, Na⁺/Cd²⁺/Mn²⁺ ions are fully disordered on the fluorite A-site with 0.25-0.25-0.5 occupancy, while the F site contains a disordered vacancy due to the 7/8 occupation in the defect fluorite structure.

Despite rather strong antiferromagnetic interactions between Ni²⁺ moments in NaCdNi₂F₇ ($\theta_{\text{CW}} = -91.2(5)$ K),

no transition is seen until a spin-glass freezing at $T_f = 3.2$ K, indicating a large magnetic frustration ($f = 28.5$) in this $S = 1$ pyrochlore antiferromagnet. A spin-glass ground-state is noted via ZFC/FC splitting of χ at T_f in a small field (100 Oe), reinforced by the frequency-dependent shift of the χ' cusp maximum, $T_f(\nu)$, to a higher temperature. This shift was well parametrized by the empirical Vogel-Fulcher law as well as the theory of dynamical scaling, with fitted parameters typical of insulating spin-glasses. Magnetic entropy of only $\sim R \ln(2)$ is recovered at 100 K, in contrast to the expected Heisenberg value for a $S = 1$ system ($R \ln(3)$), indicating large residual entropy at low temperature consistent with a ground-state with continued dynamics. This was also seen in the isostructural analogue $\text{NaCaNi}_2\text{F}_7$. [32,38,39]

$\text{NaCdMn}_2\text{F}_7$ shows weaker antiferromagnetic interactions between Mn^{2+} spins ($\theta_{\text{CW}} = -42.4(4)$ K) compared to $\text{NaSrMn}_2\text{F}_7$ ($\theta_{\text{CW}} = -89.72$ K), as the Mn-F distance in the Mn-F-Mn superexchange pathway is larger in the defect-fluorite structure compared to the $\text{NaSrMn}_2\text{F}_7$ pyrochlore. Although the FCC lattice offers weaker geometrical frustration in 3D than the pyrochlore lattice, no magnetic transition is seen until a spin-glass transition at $T_f = 2.0$ K. This is much lower than the mean-field interaction strength, yielding a large frustration index of $f \sim 21$. AC magnetic susceptibility and specific heat measurements also confirmed the glassy nature of this transition.

The spin-glass ground-states uncovered in $\text{NaCdNi}_2\text{F}_7$ and $\text{NaCdMn}_2\text{F}_7$ are in line with all the previously-studied $\text{AA}'\text{B}_2\text{F}_7$ -type pyrochlore fluorides. [29–33] The spin freezing is invoked by random local variations in magnetic bond lengths and angles – magnetic bond disorder. This comes as a result of the chemical disorder of the non-magnetic ions – the random mixing of Na/Cd on the pyrochlore A-site in $\text{NaCdNi}_2\text{F}_7$, as well as random mixing of Na/Cd/Mn ions in the defect-fluorite A-site in $\text{NaCdMn}_2\text{F}_7$. Monte Carlo simulations on the classical Heisenberg antiferromagnet with nearest neighbor exchange on the pyrochlore lattice reveal that the spin glass transition temperature correlates with the disorder strength as $k_B T_f = \sqrt{\frac{8}{3}} \Delta$, where Δ is the amplitude of small variations in the exchange coupling constant J_{ij} . [26]

Geometric magnetic frustration remains understudied in fluoride compounds, when compared to their oxide counterparts. Expanding the studies of the 2-2-7 fluorides past the border of pyrochlore structure stability provides an important comparison with the heavy rare-earth zirconate and hafnate oxides. This initial characterisation paves

the way for a more detailed investigation into the role of disorder in the geometrically frustrated pyrochlore fluoride magnets.

Acknowledgements

This work was supported by the Czech Ministry of Education, Youth and Sports (MŠMT, project no. LUABA24056), the Czech Science Foundation (project no. 19-21575Y) and the Charles University (GA UK project no. 48924). The preparation, characterization and measurement of bulk physical properties were performed in MGML (<https://mgml.eu>), which is supported within the program of Czech Research Infrastructures (project no. LM2023065). The authors additionally thank Gaël Bastien and Milan Klicpera for useful discussions.

References

- [1] A. Ramirez, *Strongly Geometrically Frustrated Magnets*, Annu. Rev. Mater. Res. **24**, 453 (1994).
- [2] J. E. Greedan, *Geometrically Frustrated Magnetic Materials*, J. Mater. Chem. **11**, 37 (2001).
- [3] J. E. Greedan, *Frustrated Rare Earth Magnetism: Spin Glasses, Spin Liquids and Spin Ices in Pyrochlore Oxides*, J. Alloys Compd. **408–412**, 444 (2006).
- [4] L. Balents, *Spin Liquids in Frustrated Magnets*, Nature **464**, 199 (2010).
- [5] L. Savary and L. Balents, *Quantum Spin Liquids: A Review*, Reports Prog. Phys. **80**, 016502 (2017).
- [6] J. Khatua, B. Sana, A. Zorko, M. Gomilšek, K. Sethupathi, M. S. R. Rao, M. Baenitz, B. Schmidt, and P. Khuntia, *Experimental Signatures of Quantum and Topological States in Frustrated Magnetism*, Phys. Rep. **1041**, 1 (2023).
- [7] B. C. Chakoumakos, *Systematics of the Pyrochlore Structure Type, Ideal A2B2X6Y*, J. Solid State Chem. **53**, 120 (1984).
- [8] M. A. Subramanian, G. Aravamudan, and G. V. Subba Rao, *Oxide Pyrochlores — A Review*, Prog. Solid State Chem. **15**, 55 (1983).
- [9] D. Reig-i-Plessis and A. M. Hallas, *Frustrated Magnetism in Fluoride and Chalcogenide Pyrochlore Lattice Materials*, Phys. Rev. Mater. **5**, 030301 (2021).
- [10] D. Bernard, J. Pannetier, and J. Lucas, *Hg2M2F6S et Hg2M2F6O: Deux Nouvelles Familles de Pyrochlores Contenant Du Mercure et Des Métaux M de Transition Divalents*, J. Solid State Chem. **14**, 328 (1975).
- [11] K. E. Sickafus, J. M. Wills, and N. W. Grimes, *Structure of Spinel*, J. Am. Ceram. Soc. **82**, 3279 (1999).
- [12] S. H. Lee et al., *Frustrated Magnetism and Cooperative Phase Transitions in Spinels*, J. Phys. Soc. Japan **79**, 1 (2010).
- [13] L. W. Masachchi, N. Keerthisinghe, G. Morrison, A. A. Berseneva, M. D. Smith, and H.-C. zur Loye, *Crystal Growth and Magnetism of Transition Metal Pyrochlore Fluorides*, Inorg. Chem. **62**, 13793 (2023).

- [14] M. V. Talanov and V. M. Talanov, *Formation of Breathing Pyrochlore Lattices: Structural, Thermodynamic and Crystal Chemical Aspects*, CrystEngComm **22**, 1176 (2020).
- [15] Y. Tanaka, M. Yoshida, M. Takigawa, Y. Okamoto, and Z. Hiroi, *Novel Phase Transitions in the Breathing Pyrochlore Lattice: 7Li-NMR on $\text{LiInCr}_4\text{O}_8$ and $\text{LiGaCr}_4\text{O}_8$* , Phys. Rev. Lett. **113**, 227204 (2014).
- [16] P. Ghosh, Y. Iqbal, T. Müller, R. T. Ponnaganti, R. Thomale, R. Narayanan, J. Reuther, M. J. P. Gingras, and H. O. Jeschke, *Breathing Chromium Spinels: A Showcase for a Variety of Pyrochlore Heisenberg Hamiltonians*, Npj Quantum Mater. **4**, 63 (2019).
- [17] J. S. Gardner, M. J. P. Gingras, and J. E. Greedan, *Magnetic Pyrochlore Oxides*, Rev. Mod. Phys. **82**, 53 (2010).
- [18] H. J. Silverstein et al., *Liquidlike Correlations in Single-Crystalline $\text{Y}_2\text{Mo}_2\text{O}_7$: An Unconventional Spin Glass*, Phys. Rev. B **89**, 054433 (2014).
- [19] S. Petit, P. Bonville, I. Mirebeau, H. Mutka, and J. Robert, *Spin Dynamics in the Ordered Spin Ice $\text{Tb}_2\text{Sn}_2\text{O}_7$* , Phys. Rev. B **85**, 054428 (2012).
- [20] T. Fennell, P. P. Deen, A. R. Wildes, K. Schmalzl, D. Prabhakaran, A. T. Boothroyd, R. J. Aldus, D. F. McMorrow, and S. T. Bramwell, *Magnetic Coulomb Phase in the Spin Ice $\text{Ho}_2\text{Ti}_2\text{O}_7$* , Science (80-.). **326**, 415 (2009).
- [21] J. S. Gardner et al., *Cooperative Paramagnetism in the Geometrically Frustrated Pyrochlore Antiferromagnet $\text{Tb}_2\text{Ti}_2\text{O}_7$* , Phys. Rev. Lett. **82**, 1012 (1999).
- [22] J. D. M. Champion et al., *$\text{Er}_2\text{Ti}_2\text{O}_7$: Evidence of Quantum Order by Disorder in a Frustrated Antiferromagnet*, Phys. Rev. B **68**, 020401 (2003).
- [23] R. Sibille et al., *Coulomb Spin Liquid in Anion-Disordered Pyrochlore $\text{Tb}_2\text{Hf}_2\text{O}_7$* , Nat. Commun. **8**, 892 (2017).
- [24] M. Klicpera, D. Staško, K. Vlášková, F. Hájek, D. Vojtasová, J. Zelenka, and R. H. Colman, *Magnetic Frustration in Rare-Earth Zirconates $\text{A}_2\text{Zr}_2\text{O}_7$, the Case of Laser Heated Pedestal Method Synthesised $\text{A} = \text{Er}, \text{Tm}, \text{Yb}, \text{and Lu}$ Single Crystals*, J. Alloys Compd. **978**, 173440 (2024).
- [25] Z. Song and Q. Liu, *Tolerance Factor, Phase Stability and Order-Disorder of the Pyrochlore Structure*, Inorg. Chem. Front. **7**, 1583 (2020).
- [26] T. E. Saunders and J. T. Chalker, *Spin Freezing in Geometrically Frustrated Antiferromagnets with Weak Disorder*, Phys. Rev. Lett. **98**, 1 (2007).
- [27] A. Andreanov, J. T. Chalker, T. E. Saunders, and D. Sherrington, *Spin-Glass Transition in Geometrically Frustrated Antiferromagnets with Weak Disorder*, Phys. Rev. B - Condens. Matter Mater. Phys. **81**, 1 (2010).
- [28] R. Hänsler and W. Rüdorff, *$\text{A}_2\text{B}_2\text{F}_7$ - Verbindungen Mit Pyrochlor- Und Weberitstruktur*, Zeitschrift Für Naturforsch. B **25**, 1306 (1970).
- [29] J. W. Krizan and R. J. Cava, *$\text{NaCaCo}_2\text{F}_7$: A Single-Crystal High-Temperature Pyrochlore Antiferromagnet*, Phys. Rev. B **89**, 214401 (2014).
- [30] J. W. Krizan and R. J. Cava, *$\text{NaSrCo}_2\text{F}_7$, a Co^{2+} Pyrochlore Antiferromagnet*, J. Phys. Condens. Matter **27**, 296002 (2015).
- [31] A. Kancko, G. Giester, and R. H. Colman, *Structural and Spin-Glass Properties of Single Crystal $\text{Jeff} = \frac{1}{2}$ Pyrochlore Antiferromagnet $\text{NaCdCo}_2\text{F}_7$: Correlating T_f with Magnetic-Bond-Disorder*, Phys. Scr. **98**, 075947 (2023).
- [32] J. W. Krizan and R. J. Cava, *$\text{NaCaNi}_2\text{F}_7$: A Frustrated High Temperature Pyrochlore Antiferromagnet with $S=1$ Ni^{2+}* , Phys. Rev. B **92**, 014406 (2015).
- [33] M. B. Sanders, J. W. Krizan, K. W. Plumb, T. M. McQueen, and R. J. Cava, *$\text{NaSrMn}_2\text{F}_7$, $\text{NaCaFe}_2\text{F}_7$, and $\text{NaSrFe}_2\text{F}_7$: Novel Single Crystal Pyrochlore Antiferromagnets*, J. Phys. Condens. Matter **29**, 045801 (2017).
- [34] M. Amirabbasi, *Ab Initio Description of Magnetic and Critical Properties of Spin-Glass Pyrochlore $\text{NaSrMn}_2\text{F}_7$* , AIP Adv. **13**, (2023).
- [35] K. A. Ross, J. W. Krizan, J. A. Rodriguez-Rivera, R. J. Cava, and C. L. Broholm, *Static and Dynamic XY-like Short-Range Order in a Frustrated Magnet with Exchange Disorder*, Phys. Rev. B **93**, 014433 (2016).
- [36] K. A. Ross, J. M. Brown, R. J. Cava, J. W. Krizan, S. E. Nagler, J. A. Rodriguez-Rivera, and M. B. Stone, *Single-Ion Properties of the $\text{Seff} = 1/2$ XY Antiferromagnetic Pyrochlores $\text{NaA}'\text{Co}_2\text{F}_7$ ($\text{A}' = \text{Ca}^{2+}, \text{Sr}^{2+}$)*, Phys. Rev. B **95**, 144414 (2017).
- [37] J. Zeisner et al., *Magnetic Interactions and Spin Dynamics in the Bond-Disordered Pyrochlore Fluoride $\text{NaCaCo}_2\text{F}_7$* , Phys. Rev. B **99**, 155104 (2019).
- [38] Y. Cai et al., *MSR Study of Spin Freezing and Persistent Spin Dynamics in $\text{NaCaNi}_2\text{F}_7$* , J. Phys. Condens. Matter **30**, 385802 (2018).
- [39] K. W. Plumb, H. J. Changlani, A. Scheie, S. Zhang, J. W. Krizan, J. A. Rodriguez-Rivera, Y. Qiu, B. Winn, R. J. Cava, and C. L. Broholm, *Continuum of Quantum Fluctuations in a Three-Dimensional $S = 1$ Heisenberg Magnet*, Nat. Phys. **15**, 54 (2019).
- [40] S. Zhang, H. J. Changlani, K. W. Plumb, O. Tchernyshyov, and R. Moessner, *Dynamical Structure Factor of the Three-Dimensional Quantum Spin Liquid Candidate $\text{NaCaNi}_2\text{F}_7$* , Phys. Rev. Lett. **122**, 167203 (2019).
- [41] CrysAlisPro, Oxford Diffraction, Agilent Technologies UK Ltd, England.
- [42] L. Palatinus and G. Chapuis, *SUPERFLIP - A Computer Program for the Solution of Crystal Structures by Charge Flipping in Arbitrary Dimensions*, J. Appl. Crystallogr. **40**, 786 (2007).
- [43] V. Petříček, L. Palatinus, J. Plášil, and M. Dušek, *Jana2020 – a New Version of the Crystallographic Computing System Jana*, Zeitschrift Für Krist. - Cryst. Mater. **238**, 271 (2023).
- [44] K. Momma and F. Izumi, *VESTA : A Three-Dimensional Visualization System for Electronic and Structural Analysis*, J. Appl. Crystallogr. **41**, 653 (2008).
- [45] A. A. Coelho, *TOPAS and TOPAS-Academic : An Optimization Program Integrating Computer Algebra and Crystallographic Objects Written in C++*, J. Appl. Crystallogr. **51**, 210 (2018).
- [46] D. Staško, K. Vlášková, D. Vojtasová, F. Hájek, P. Král, R. H. Colman, and M. Klicpera, *The Synthesis of the Rare Earth $\text{A}_2\text{Zr}_2\text{O}_7$ Single Crystals by Simplified Laser-Heated Floating Hot Zone and Pedestal Methods*, Mater. Today Chem. **39**, (2024).
- [47] R. D. Shannon, *Revised Effective Ionic Radii and Systematic Studies of Interatomic Distances in Halides and Chalcogenides*, Acta Crystallogr. Sect. A **32**, 751 (1976).

- [48] E. C. Koskelo, P. Mukherjee, C. Liu, A. C. Sackville Hamilton, H. S. Ong, C. Castelnovo, M. E. Zhitomirsky, and S. E. Dutton, *Comparative Study of Magnetocaloric Properties for Gd³⁺ Compounds with Different Frustrated Lattice Geometries*, PRX Energy **2**, 1 (2023).
- [49] J. A. Mydosh, *Spin Glasses: An Experimental Introduction* (Taylor & Francis, 1993).
- [50] J. Souletie and J. L. Tholence, *Critical Slowing down in Spin Glasses and Other Glasses: Fulcher versus Power Law*, Phys. Rev. B **32**, 516 (1985).
- [51] P. w. Anderson, B. I. Halperin, and c. M. Varma, *Anomalous Low-Temperature Thermal Properties of Glasses and Spin Glasses*, Philos. Mag. **25**, 1 (1972).